Investigation of Electrode Kinetics of Porous La-Sr-Co-Fe-oxide (LSCF) Electrodes on Yttria-Stabilized Zirconia (YSZ) Electrolyte Using Alternating Current (AC) and Direct Current (DC) Methods

Journal of The Electrochemical Society, 2021 **168** 064510
1945-7111/2021/168(6)/064510/13/$40.00 © 2021 The Electrochemical Society ("ECS"). Published on behalf of ECS by IOP Publishing Limited

Investigation of Electrode Kinetics of Porous La-Sr-Co-Fe-oxide (LSCF) Electrodes on Yttria-Stabilized Zirconia (YSZ) Electrolyte Using Alternating Current (AC) and Direct Current (DC) Methods

Chong Lei, Michael F. Simpson,[z] and Anil V. Virkar[*]

Department of Materials Science and Engineering, University of Utah, Salt Lake City, Utah 84112, United States of America

Lanthanum strontium cobalt iron oxide (LSCF) is commonly used as a cathode in solid oxide fuel cells (SOFCs), because it is a mixed ionic-electronic conductor with reasonable oxygen ion conductivity and high electronic conductivity. Yttria stabilized zirconia (YSZ) is used as an electrolyte in SOFCs with good oxygen ion conductivity. AC techniques are used to test the performance of SOFCs. But electrode processes at the cathode and the anode cannot be studied separately using two-electrode electrical impedance spectroscopy (EIS). To overcome this problem, two-electrode EIS with three probes and DC tests were conducted. An LSCF/8YSZ/LSCF symmetrical bar-shaped cell was made, and platinum strip electrodes were applied as probes for EIS and DC measurements. Impedance spectra across the cathode and the platinum strip electrode and across the anode and the platinum strip electrode were measured separately. The sum was evaluated to see if it matches the EIS spectra across the cathode and the anode. The polarity was switched to study how it affects the electrode processes. The polarization resistances of the electrodes were also measured by a DC method separately. EIS and DC measurements are in good agreement. Results indicate the two electrodes need not be identical.
 [DOI: 10.1149/1945-7111/ac0946]

Manuscript submitted April 5, 2021; revised manuscript received May 17, 2021. Published June 16, 2021.

Development of solid oxide fuel cells (SOFCs) is of great significance because of the increasing demand for clean energy.[1–4] SOFCs are electrochemical devices that can convert the chemical energy of oxidation of a fuel gas such as H_2, methane, and natural gas into electrical energy efficiently.[5–9] Porous cathode, dense electrolyte, and porous anode are the three main parts of typical SOFCs. In SOFCs, solid oxide materials with good oxygen ion conductivity are used as the electrolyte, which conducts oxygen ions from the cathode to the anode. Usually, SOFCs exhibit good performance at a temperature ranging from 700 to 1000 °C, since most electrolytes do not exhibit sufficient oxygen ion conductivities at low temperatures.[10] The most common electrolyte used in SOFCs is the 8 mol% Y_2O_3 stabilized ZrO_2 (8YSZ), which has good oxygen ion conductivity at typical SOFCs operating temperatures (>800 °C).[11–14] The fundamental requirements for electrodes in SOFCs are good electronic conductivity, good catalytic activity, and high oxygen ion diffusivity.[15–17] A mixed ionic-electronic conductor (MIEC)-lanthanum strontium cobalt iron oxide (LSCF) is attracting attention for use in SOFCs as a cathode, because it has good electronic conductivity (~300 Scm^{-1} at 700 °C) and reasonable oxygen ion conductivity (~1.2×10^{-2} Scm^{-1} at 700 °C).[15,18]

Figure 1 shows a schematic of the electrode reaction that occurs in MIEC and oxygen concentration profile in the porous MIEC. Oxygen diffuses through the porous electrode, and the electrode redox reaction $O + ne^- \rightleftarrows R$ occurs over the surface area of the porous electrode and the three-phase boundary (TPB), which is the line spread out in three dimensions (narrow, of undefined width) between the electrode, the electrolyte, and the gas phase.[19] In this case, because of the low ionic conductivity of LSCF compared to YSZ, most of the reaction is expected to occur near the electrolyte/electrode interface along the electrolyte, the electrode and the gas phase boundary. Cells with symmetrical electrodes are widely used to study electrode kinetics, and both electrodes are assumed to exhibit nearly identical performance.[13,20] However, the electrodes need not be identical under load. There is no fundamental reason why reactions $\frac{1}{2}O_2 + 2e' \rightarrow O^{2-}$ and $O^{2-} \rightarrow \frac{1}{2}O_2 + 2e'$ should exhibit the same kinetics. Electrochemical impedance spectroscopy (EIS) is a commonly used technique to study the electrochemical performance of SOFCs and SOFC electrodes. However, by using the typical two-electrode EIS on symmetrical cells, the polarization resistances of the cathode and the anode cannot be measured separately, though they are sometimes assumed to be the same. Thus, two-electrode EIS needs to be conducted using two electrodes and one pseudo-reference electrode. The pseudo-reference electrode is located in the middle of the working electrode and the counter electrode. Szendrei et al.[21] reported a three/four-probe EIS measurement with one/two pseudo-reference electrodes embedded in a proton exchange membrane fuel cell. The electrochemical performance of the two electrodes was evaluated separately by EIS, and the sum of the spectra across the two electrodes and one of the two pseudo-reference electrodes were in good agreement with the spectra across the entire cell.

SOFCs operate in a DC mode. In many complex cases, EIS spectra can be fitted to multiple equivalent circuits thus making the determination of a unique set of parameters difficult.[20,22] Thus, DC techniques are also important for study of electrochemical performance of electrodes.[22,23] In typical studies, thin electrolytes are used to make symmetrical cells, which makes it difficult to measure the polarization resistance of the cathode and the anode separately. In the present work, an LSCF/8YSZ/LSCF bar-shaped sample was made with symmetrical porous LSCF electrodes applied on both sides of the 8YSZ bar with a strip of platinum painted at the mid-point of the bar used as a pseudo-reference electrode. This allowed the measurement of polarization resistances of the cathode and the anode separately. The electrode kinetics was investigated by using both EIS and DC techniques. Also, because of the very large ohmic contribution in the bar-shaped sample, the current density is expected to be very low. This also allows a study of electrode kinetics at exceptionally low current densities, well below the exchange current density. This thus allows one to explore the regime, generally not accessible using thin disk samples.

Experimental

Figure 2 shows a schematic of the LSCF/8YSZ/LSCF bar, which was fabricated first by pressing 8YSZ powder (Tosoh, TZ-8Y) in a bar-shaped die, and then sintering in air at 1600 °C for 4 h. The density of the sintered YSZ bar was measured by the Archimedes method. LSCF ($(La_{0.6}Sr_{0.4})_{0.95}Co_{0.2}Fe_{0.8}O_{3-x}$) powder (Fuel Cell Materials, LSCF-HP) was painted on both ends of the bar and fired in air at 1000 °C for 1 h. Platinum strip electrodes (P1, P2, P3), about 1.5 mm wide, were circumferentially applied along the length of the bar at three different places and fired at 900 °C for 1 h. For comparison and contrast, a disk-shaped LSCF/8YSZ/LSCF cell was made using the same method but without platinum strip electrodes.

*Electrochemical Society Fellow
[z]E-mail: michael.simpson@utah.edu

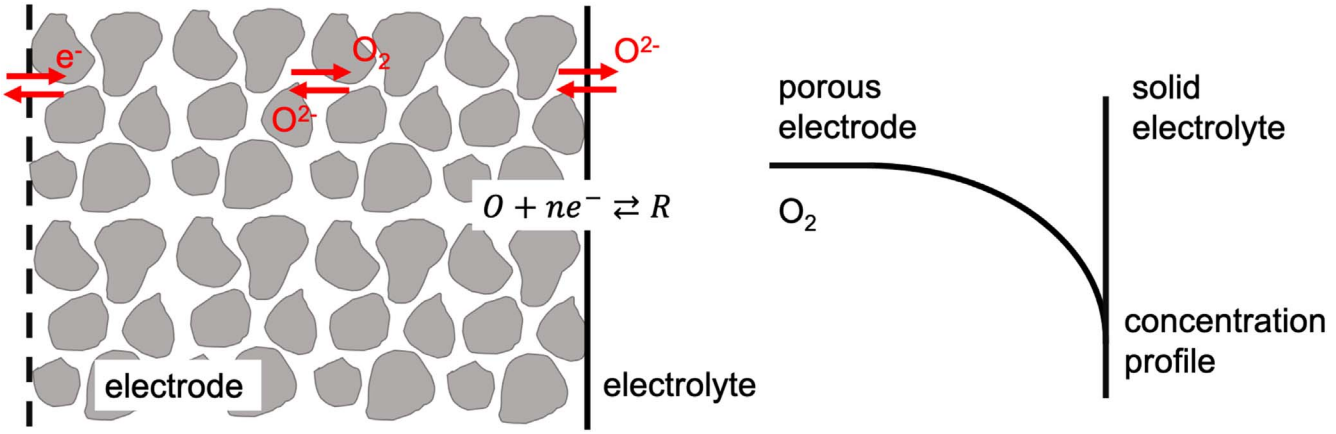

Figure 1. A schematic of the electrode reaction and oxygen concentration profiles that occur with an MIEC electrode.

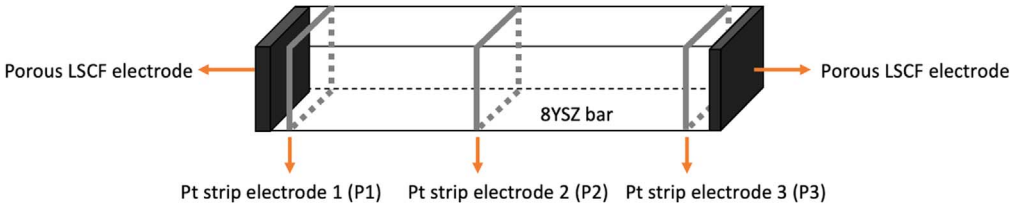

Figure 2. A schematic of the LSCF/8YSZ/LSCF bar sample, ~4.0 cm in length, ~1.0 cm in width, and ~0.9 cm in thickness.

XRD patterns were obtained using an X-ray diffractometer (Bruker D2 Phaser) with Cu kα radiation to determine the phases present in LSCF. The morphology of the porous LSCF electrode was examined by using a scanning electron microscope (FEI Nova Nano SEM 630). Both EIS and DC tests were used for electrical testing of the LSCF/8YSZ/LSCF bar sample. Gold mesh was applied on the porous LSCF electrodes and fired at 500 °C for 1 h. Platinum wires were attached to the platinum strip electrodes and the gold mesh. The sample was placed in a tubular furnace with the platinum wires protruding out; the platinum wires were isolated using ceramic tubes. AC tests were also performed by EIS using a Solartron electrochemical interface (SI 1287) and an impedance/gain-phase analyzer (SI 1260) using a two-electrode method with three probes over a temperature range from 600 °C to 800 °C. The range of frequencies tested was from 1 Hz to 1 MHz, with an amplitude of 10 mV. Similar EIS tests were performed on the LSCF/8YSZ/LSCF disk-shaped sample. To measure the resistivity of the 8YSZ bar, a DC voltage of 0.36V was applied across the sample. The corresponding current and the voltages across each platinum strip electrode were measured. For DC electrochemical tests, voltage ranging from 0.05–0.36 V was applied across the sample. The upper voltage was set to 0.36 V, well below the decomposition potential, so that no changes in stoichiometry of YSZ near the electrodes is expected. At each value of the applied DC voltage, the corresponding current and the voltage across each end electrode and the platinum strip electrode P2 were measured by Keithley 2000 meters. This allowed measurement of the polarization resistance of each end electrode separately.

Relevant Equations

Figure 3a shows schematic impedance spectra of a typical electrolyte/electrodes system, which can be described as a sum of the grain impedance (Z_g), the grain boundary impedance (Z_{gb}), and the electrode impedance (Z_e):

$$Z_{cell} = Z_g + Z_{gb} + Z_e \qquad [1]$$

Figure 3b is a simplified equivalent circuit that can describe the impedance spectra in Fig. 3a.

To study the behavior of the two electrodes separately, a two-electrode EIS was used. A DC bias was applied across the cell, which is external to the AC measurement hardware. The EIS spectra across the electrode and the reference electrode can be measured, where the reference electrode was used to isolate the other part of the loaded cell.[21] Schematics are shown in Fig. 4. EIS spectra across the two electrodes can be measured as shown in Fig. 4a. By using the two-electrode method with three probes, the impedance across each electrode and probe (P2) can be measured as shown in Figs. 4b and 4c, respectively.

As stated previously, EIS tests are commonly used to investigate the electrochemical performance of fuel cells, while fuel cells are used in a DC mode. To measure the polarization resistance, a DC test was also used. Figure 5 shows a schematic of the DC test. The polarization resistances of the two electrodes are denoted by R_{EL} and R_{ER}. The overpotentials at the end electrodes EL and ER are denoted η_{EL} and η_{ER}, respectively. The polarization resistances of the Pt strip electrodes are negligible, since the input resistance of the measuring meter is quite large ($\geqslant$10 GΩ), which means negligible current flows through the measuring meter.[21] The resistivity of the YSZ bar (ρ) was measured by using a 3-point DC method. Thus, the overpotential is given by.

$$\eta_{EL} = V_{EL-P2} - \rho\frac{l_{RYSZ1}}{A}I \qquad [2]$$

where V_{EL-P2} is the measured potential across EL and P2, ρ is the measured ionic resistivity of the YSZ bar, l_{RYSZ1} is the distance between EL and P2, A is the cross-sectional area of the YSZ bar, and I is the measured current. Similar equation was also applied to ER. V_{EL-P2} and V_{ER-P_2} measurements were made over a range of current densities. The overpotential could then be calculated from Eq. 2 and plotted as a function of current density. The polarization resistance can then be calculated by Ohm's law.

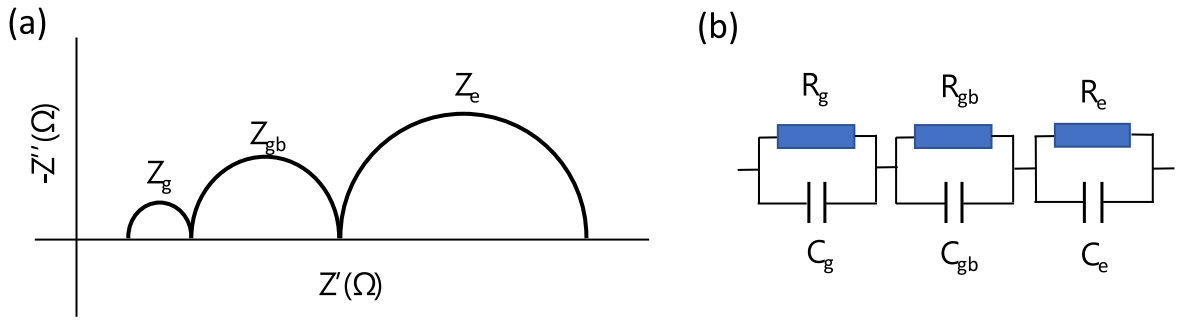

Figure 3. (a) A schematic of the impedance spectra of a typical electrolyte/electrodes system. (b) An equivalent circuit to describe the impedance spectra.

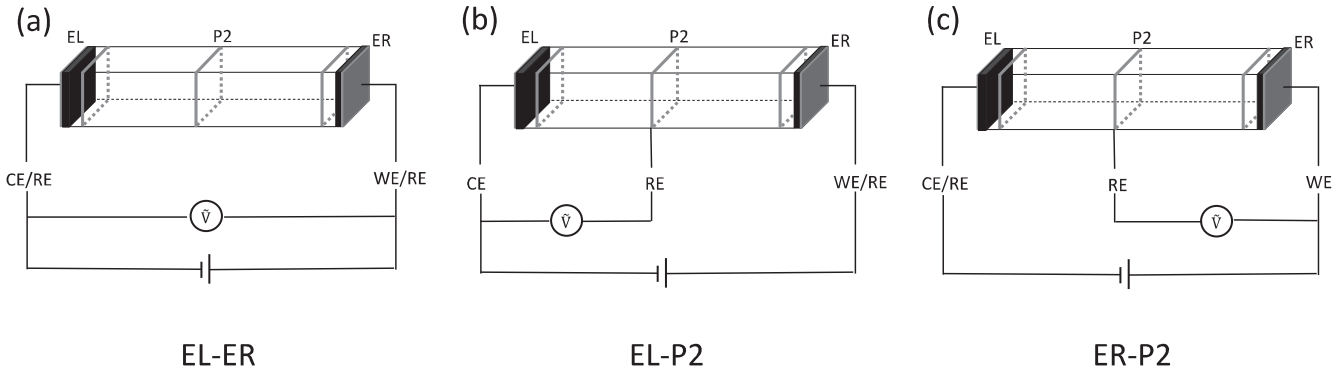

Figure 4. Schematics, showing (a) the application of an AC signal across the cell, EL and ER, (b) across EL (cathode) and P2 (reference electrode), and (c) across ER (anode) and P2 (reference electrode).

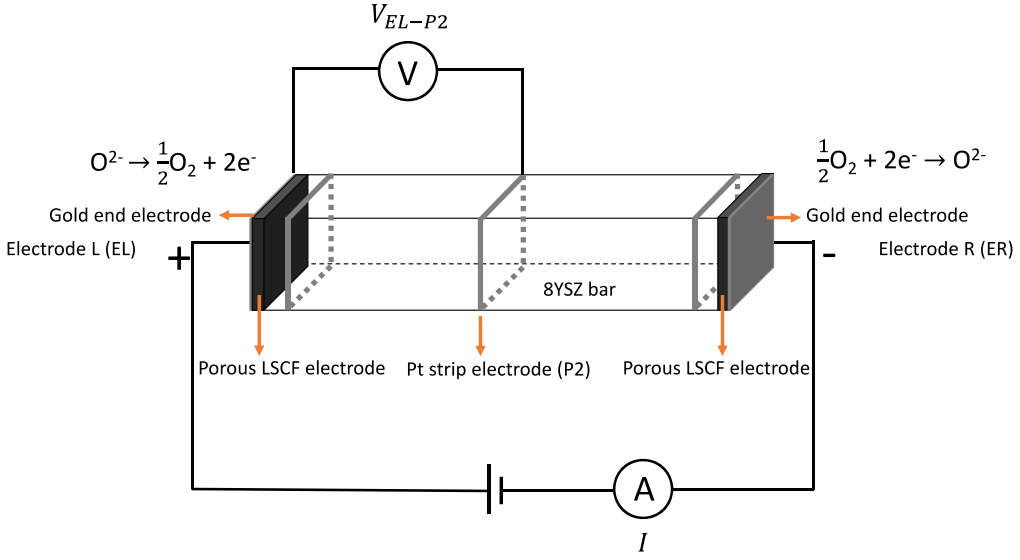

Figure 5. A schematic of the DC test across the YSZ bar.

Results and Discussion

The measured density of the sintered YSZ sample was 5.93 gcm^{-3}, which is >99% of the theoretical density. With such a high relative density achieved, it was deemed suitable for EIS and DC tests. The 8YSZ bar is about 4.0 cm in length, 1.0 cm in width, and 0.9 cm in thickness. The widths of the Pt strips were about 1.5 mm. Figure 6 shows an XRD pattern of the LSCF sample fired at 1000 °C for 1h; a pure perovskite crystal structure was obtained.

Figures 7a, 7b shows scanning electron microscope (SEM) images of LSCF electrode fired at 1000 °C. It is clear that a porous microstructure can be obtained when LSCF is fired at this temperature. Figures 7c shows a cross-sectional SEM image of the porous LSCF electrode on a dense YSZ electrolyte. Although the formation of $SrZrO_3$ was not observed, it is possible that a very thin layer of $SrZrO_3$ may have formed at the LSCF-YSZ interface.

Three probes were used to study the EIS spectra across any two electrodes of the LSCF/8YSZ/LSCF bar sample, separately. Figure 8 shows the impedance spectra across EL and ER (black), across EL and P2 (red), across ER and P2 (blue), and a point by point sum of spectra across EL and ER (green) for the LSCF/8YSZ/LSCF bar at (a), (b) 800 °C, (c), (d) 700 °C and (e), (f) 600 °C with different

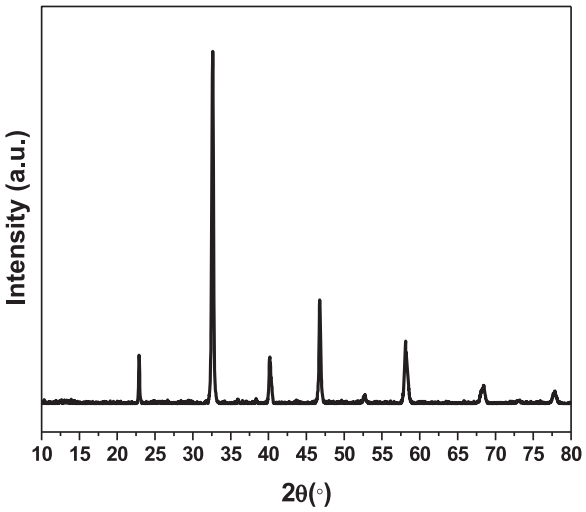

Figure 6. An XRD pattern of LSCF fired at 1000 °C for 1 h.

polarities (a), (c), (e) EL(−) and ER(+), (b), (d), (f) EL(+) and ER (−). For (a), (c), (e), EL is the cathode, which is connected to the negative terminal, where the oxygen reduction reaction (ORR) occurs. ER is the anode, which is connected to the positive terminal, where the oxygen evolution reaction (OER) occurs. By contrast, for (b), (d), (f)), EL is the anode, which is connected to the positive terminal, where the OER occurs. ER is the cathode, which is connected to the negative terminal, where the ORR occurs. Leads inductance/resistance was not removed from these spectra since its contribution was much smaller than the sample impedance, thus making little difference in the spectra. The impedance spectra across EL and P2 (red) compared to across ER and P2 (blue) are not the same, regardless of the temperature and polarity. It is seen that the polarization resistances of the two electrodes EL and ER are not identical. The spectra across EL and P2 (red) and across ER and P2 (blue) shown in Figs. 8a, 8c, 8e and the spectra across EL and P2 (red) and across ER and P2 (blue) shown in Figs. 8b, 8d, 8f are almost the same when compared at the same temperature, which indicates that the polarization resistance of each electrode does not change very much when the polarity is switched. This means, at least under these conditions, $\frac{1}{2}O_2 + 2e' \rightarrow O^{2-}$ and $O^{2-} \rightarrow \frac{1}{2}O_2 + 2e'$ exhibit similar kinetics. These results are quite different than observed by Szendrei et al.[23] on (La-Sr-Mn-oxide) LSM + YSZ electrodes. Szendrei et al.[23] did not change polarities, but observed a large difference in the polarization resistances of $\frac{1}{2}O_2 + 2e' \rightarrow O^{2-}$ and $O^{2-} \rightarrow \frac{1}{2}O_2 + 2e'$ reactions. In 100% O_2 and at 610 °C, Szendrei et al.[23] measured specific polarization resistance of ∼1056 Ωcm^2 for the ORR while that for the OER, it was ∼136 Ωcm^2. Thus, it does appear that the polarization resistances for the two reactions can be quite different, depending upon the specific electrodes used.

Only at high frequencies, the spectra change when the polarity switches, since the lead inductances can change due to small twists and turns that can occur in repeat measurements.[24] The polarity does not affect the polarization resistance of each electrode. The polarization resistances increased with decreasing temperature. The high frequency intercepts indicate that the electrolyte resistance across EL and P2 (red) is slightly larger than that across ER and P2 (blue) at different temperatures, since the distance between EL and P2 is slightly larger (by ∼0.3 cm) than that between ER and P2. Also, the high frequency intercepts indicate that the electrolyte resistance across the whole sample increases with decreasing temperature, as expected. A point-by-point sum of the spectra across EL-P2 and across ER-P2 (green) almost exactly matches the spectra across EL and ER (black) at different temperatures and different polarities. Only small mismatches were observed at very high frequencies since the inductances are different because of different lengths and some small twists of the wires.

In support of using Eq. 2 with DC tests to determine polarization resistances, Fig. 9 shows the resistance of the 8YSZ bar as a function of distance, measured between the three platinum strip electrodes at (a) 800 °C, (b) 700 °C, and (c) 600 °C. The voltage applied across the two LSCF electrodes was 0.36V. The slope gives the YSZ resistance per unit length, which is 35.7 Ωcm^{-1}, 94.8 Ωcm^{-1}, and 362.7Ωcm^{-1} at 800°, 700°, and 600 °C, respectively. The intercepts (when extrapolated to zero length-figure gives data for lengths between 1 cm and 4 cm) are not zero, since the strip electrodes are quite wide, which introduces some uncertainty in the measurement of distance between probes. At 800 °C, for example, uncertainty per strip corresponds to ∼5.25 Ω, while at 600 °C, it corresponds to ∼54.3 Ω. However, the uncertainties caused by the wide platinum strip electrodes are considered to be in the acceptable range. The resistivities of YSZ at different temperatures were determined, which are 30.7, 81.6, and 312.0 Ωcm at 800, 700, and 600 °C, respectively. The measured resistivities are in good agreement with the previously reported values.[25,26] The resistivities were used to calculate the overpotential using Eq. 2.

The Butler-Volmer equation is shown below

$$i = i_o\left\{\exp\left[\frac{(1-\alpha)zF\eta}{RT}\right] - \exp\left[-\frac{\alpha zF\eta}{RT}\right]\right\} \qquad [3]$$

where i is the electrode current density, i_o is the exchange current density, α is the transfer coefficient, z is the number of electrons participating in the electrode reaction, F is the Faraday constant, η is the activation overpotential, R is the universal gas constant, and T is the absolute temperature. There are two limiting cases of the Butler-Volmer equation. In the low overpotential region, the Butler-Volmer

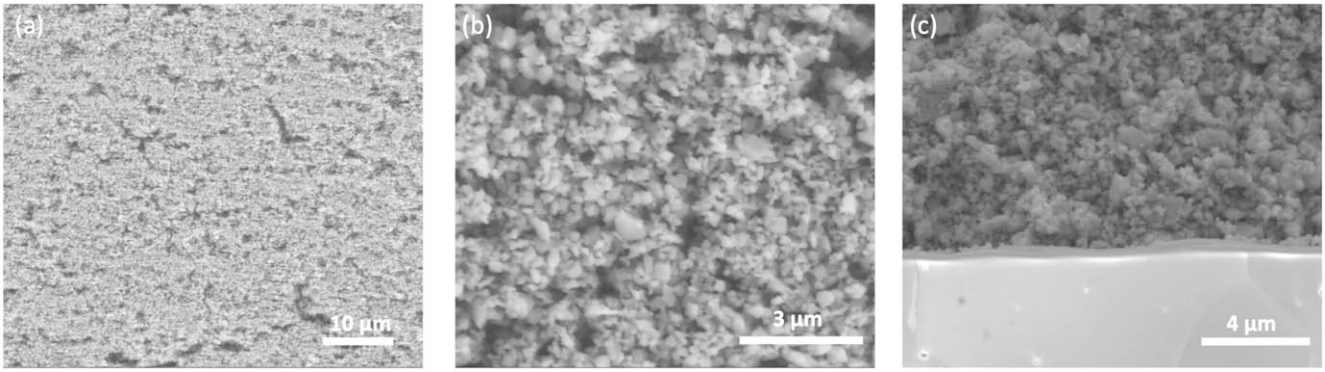

Figure 7. (a), (b) SEM images of LSCF electrode fired at 1000 °C. (c) Cross-sectional SEM image of LSCF on YSZ substrate.

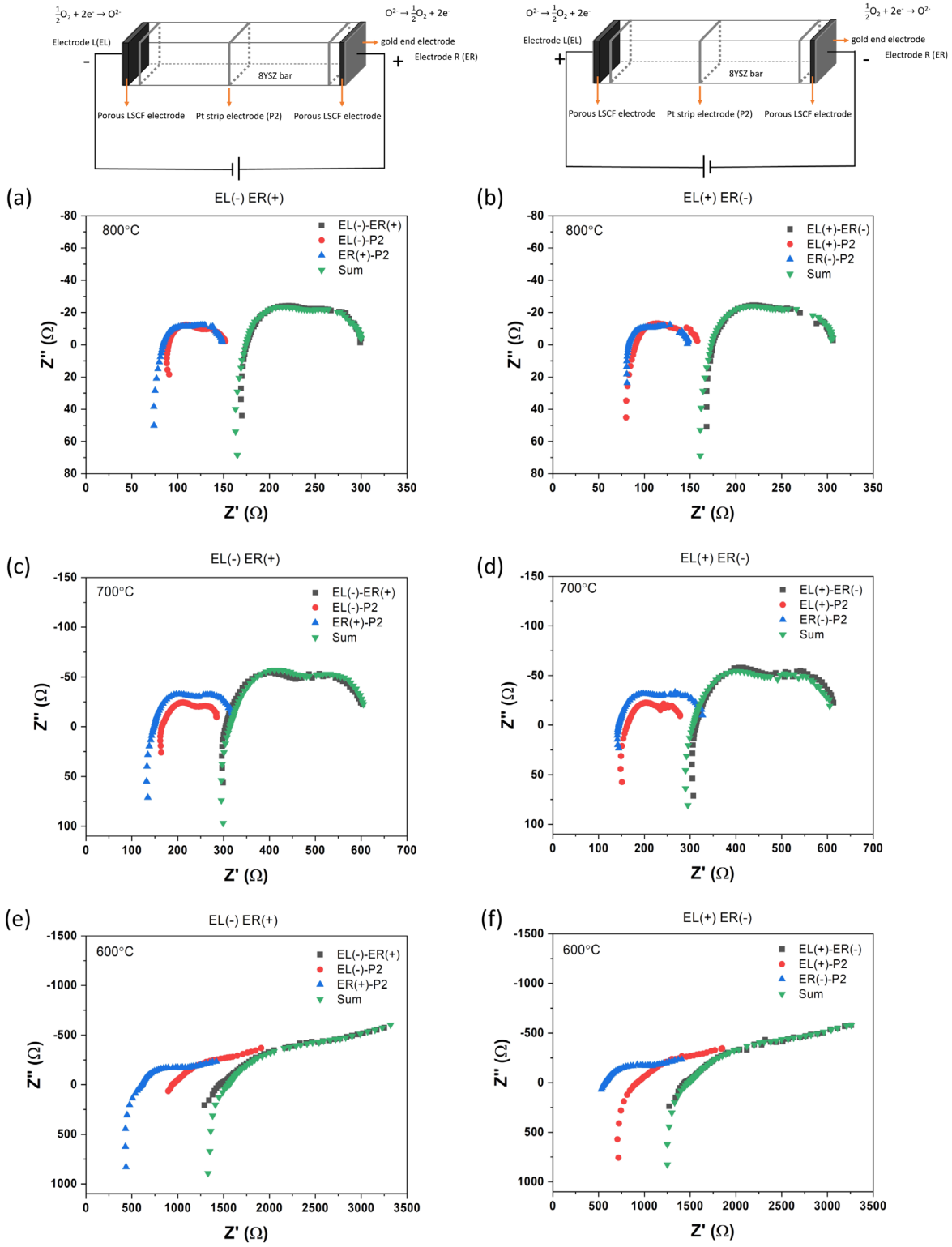

Figure 8. Impedance spectra across EL and ER (black), EL and P2 (red), ER and P2 (blue), and point by point sum of spectra across EL and ER (green) for the LSCF/8YSZ/LSCF bar at (a), (b) 800 °C, (c), (d) 700 °C and (e), (f) 600 °C with different polarities (a), (c), (e) EL(−) and ER(+), (b), (d), (f) EL(+) and ER(−). The leads resistance/inductance was not removed from these spectra.

equation can be simplified to

$$i = i_o \frac{zF}{RT}\eta \qquad [4]$$

in which the exponential terms in the Butler-Volmer equation are expanded in a Taylor series and only linear terms are retained. The exchange current density, is thus given by

$$i_0 = \frac{RT}{zFR_{ct}} \qquad [5]$$

where the area specific electrode polarization resistance R_{ct} is constant at a given temperature and in a given atmosphere. This

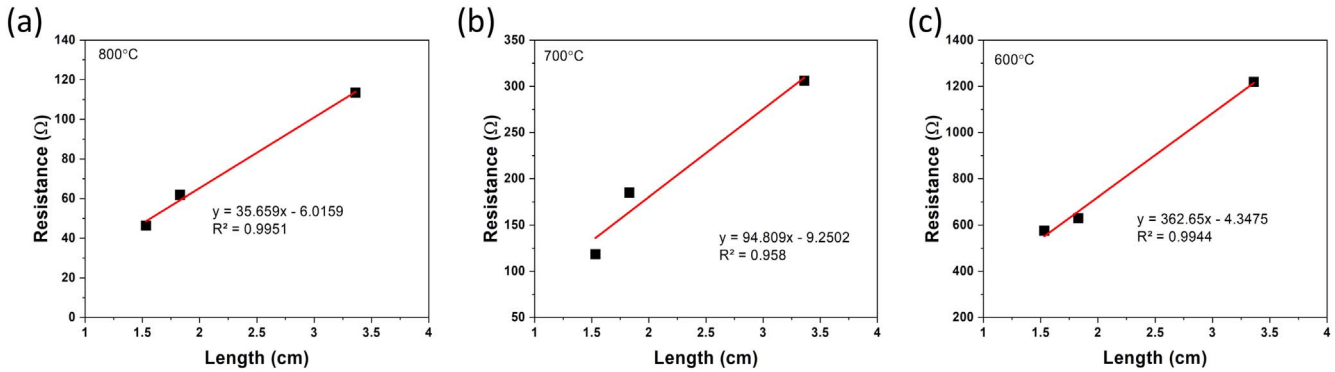

Figure 9. Resistance as a function of distance, measured between the three platinum strip electrodes at (a) 800 °C, (b) 700 °C, and (c) 600 °C.

relation is typically applicable at operating current densities on the order of i_o or several times of i_o. In the high overpotential region, Tafel behavior is often observed and the Butler-Volmer equation can be simplified to

$$\eta = -\frac{RT}{(1-\alpha)zF}\ln i_o + \frac{RT}{(1-\alpha)zF}\ln i = a + blni \qquad [6]$$

where the Tafel coefficients are given as

$$a = -\frac{RT}{(1-\alpha)zF}\ln i_o \quad b = \frac{RT}{(1-\alpha)zF} \qquad [7]$$

The above coefficients are given for anodic current. For cathodic current, the Tafel coefficients are given by

$$a = \frac{RT}{\alpha zF}\ln i_o \; b = -\frac{RT}{\alpha zF} \qquad [8]$$

In the above current densities and overpotentials correspond to their magnitudes. Equation 2 was used for calculating the overpotential. Figure 10 shows overpotential vs current density for EL (a), (c), (e) and ER (b), (d), (f) at different temperatures when EL is the cathode where the ORR occurs and ER is the anode where the OER occurs. All of the plots appear linear, and good linear fits were obtained with all of the $R^2 > 0.99$ although some nonlinearity (convex up) is apparent in the data at 600 °C. The slope gives the polarization resistance. The intercepts are expected to be zero. However, they are not zero for all of the fits given in Fig. 10. Wide platinum strip electrodes can lead to uncertainties in the accurate measurement of the YSZ resistance, which can contribute to uncertainty in the measurement of the ohmic contribution.[23] At 800 °C, the specific polarization resistances of EL and ER are 90.3 Ωcm^2 and 82.0 Ωcm^2, respectively. At 700 °C, the specific polarization resistances of EL and ER are 127.6 Ωcm^2 and 169.6 Ωcm^2, respectively. At 600 °C, the specific polarization resistances of EL and ER are 1016.2 Ωcm^2 and 1425.9 Ωcm^2, respectively. Apparently, the polarization resistances for EL and ER are different, although uncertainties related to the ohmic part could be a possible source. Note that the specific polarization resistances are exceptionally large. The reasons for this will be discussed later. Both of them increased with decreasing temperature, consistent with expectations. At 700 °C and 600 °C, EL has a lower specific polarization resistance than that of ER. At 800 °C, ER and EL specific polarization resistances are close to each other and relatively small. Error may have been introduced from uncertainty in the YSZ resistance measurement.

Figure 11 shows overpotential vs current density for EL (a), (c), (e)) and ER (b), (d), (f) at different temperatures when EL is the anode where the OER occurs and ER is the cathode where the ORR occurs. After the polarities of EL and ER were switched, these plots are also linear. Again, linear fits were applied to all of the plots. Good linear fits were obtained with all of the $R^2 > 0.99$ (again, some nonlinearity is observed at 600 °C). However, the intercepts again are not zero, and errors are assumed to be caused by the wide platinum strip electrodes. In fact, in some unpublished work on LSM + YSZ electrodes where the platinum probes were narrow (applied using a toothpick) and the intercepts were zero. At 800 °C, the specific polarization resistances for EL and ER are 78.1 Ωcm^2 and 92.9 Ωcm^2, respectively. At 700 °C, the specific polarization resistances for EL and ER are 120.3 Ωcm^2 and 167.4 Ωcm^2, respectively. At 600 °C, the specific polarization resistances for EL and ER are 1020.3 Ωcm^2 and 1377.1 Ωcm^2, respectively. Once again these are in the same range as given in Fig. 10. Note that the maximum current density is only ~1.4 $mAcm^{-2}$ at 800 °C and ~0.1 $mAcm^{-2}$ at 600 °C.

For comparison and contrast, EIS was also conducted on a disk-shaped symmetrical LSCF/8YSZ/LSCF cell. The YSZ disk thickness of the LSCF/8YSZ/LSCF sample was ~0.8 mm, and the electrode surface area was ~1 cm^2. Figure 12a shows the impedance spectra across the entire sample of the disk-shaped LSCF/8YSZ/LSCF sample, including the leads resistance/inductance over a temperature range from 600 to 800 °C; an enlarged view of the high frequency region is shown in (b). Two semi-circles are observed, and a tail at the very high frequency is observed because of the leads resistance/inductance. The leads resistance/inductance needs to be subtracted point by point to obtain a more accurate assessment of the electrodes/sample EIS spectra.[2,24,27] The EIS spectra of the leads resistance/inductance are shown in (c); the resistance of the leads increases with increasing temperature since the leads are of metallic (Pt). The Impedance spectra across the entire sample of the disk-shaped LSCF/8YSZ/LSCF without the leads resistance/inductance over a temperature range from 600 to 800 °C are shown in (d), and an enlarged view of the high frequency region is shown in (e). They were obtained by point by point subtraction of the leads resistance/inductance. After subtraction of the leads resistance/inductance, there is an incomplete arc appearing at very high frequencies, which is the impedance contribution from the YSZ. The grain size of the YSZ was several microns (see Fig. 7c). Thus, the grain boundary contribution is negligible, also since all measurements were conducted at or above 600 °C. It is clear that for the disk-shaped symmetrical LSCF/8YSZ/LSCF cell, the polarization resistance is much lower than that for the bar-shaped symmetrical LSCF/8YSZ/LSCF cell. This is because the current density i is much lower in the bar sample than the exchange current density i_0 in Eq. 3. The measured polarization resistance from EIS is ~5.2 Ωcm^2 (per each electrode) at 800 °C. The exchange current density is calculated as ~4.2 $mAcm^{-2}$. This shows that the exchange current density is much greater than the current densities measured on the bar sample. Thus, the current density regime explored using the bar sample is much lower than the exchange current density. It is well known that while the overpotential increases with net current density, the derivative of overpotential with respect to current density decreases with increasing current density. It is expected, therefore, that the measured

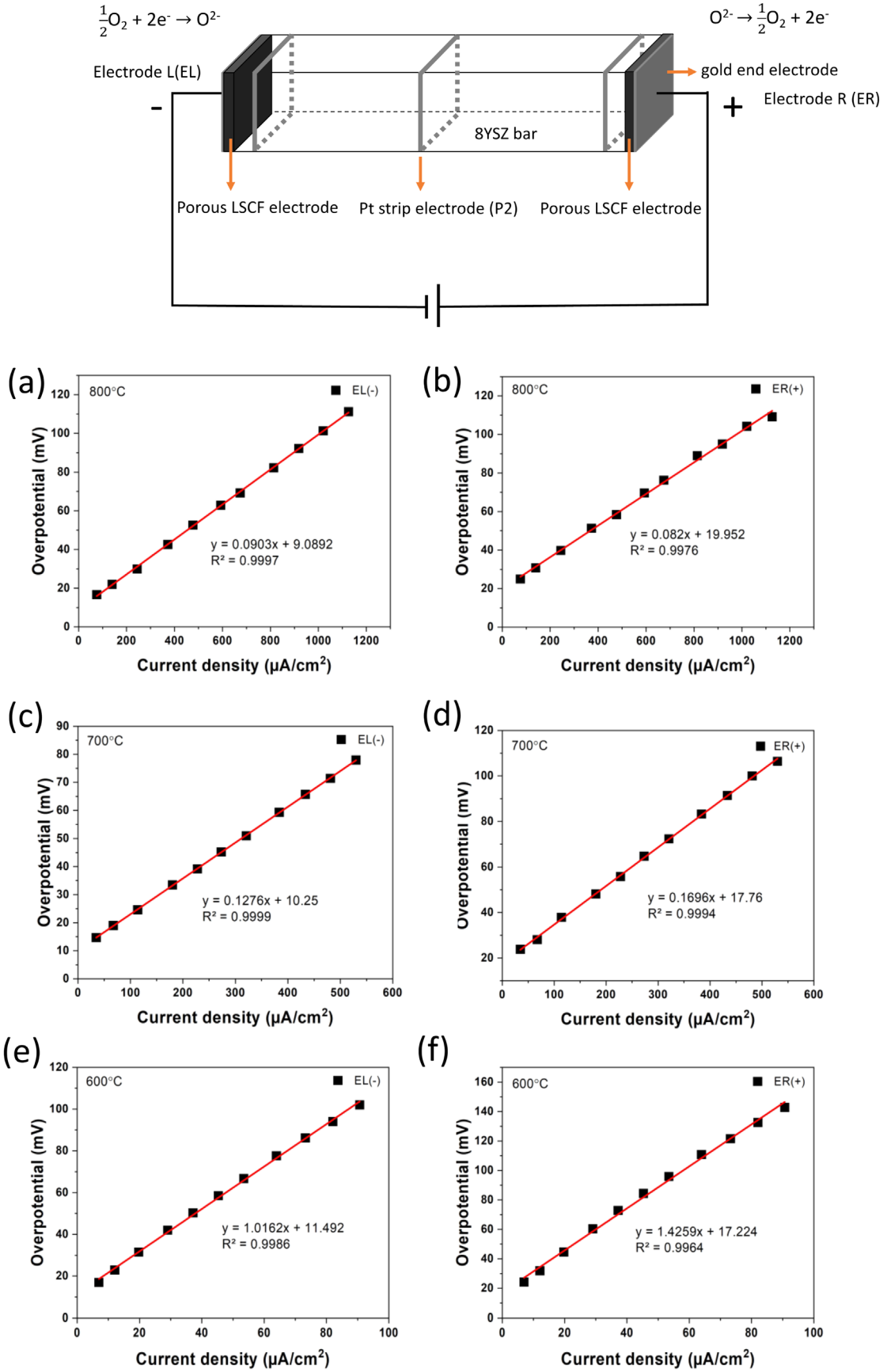

Figure 10. Overpotential vs current density for (a), (c), (e) EL (cathode), and (b), (d), (f) ER (anode) at (a), (b) 600 °C, (c), (d) 700 °C, and (e), (f) 800 °C with the polarity of EL(−) and ER(+).

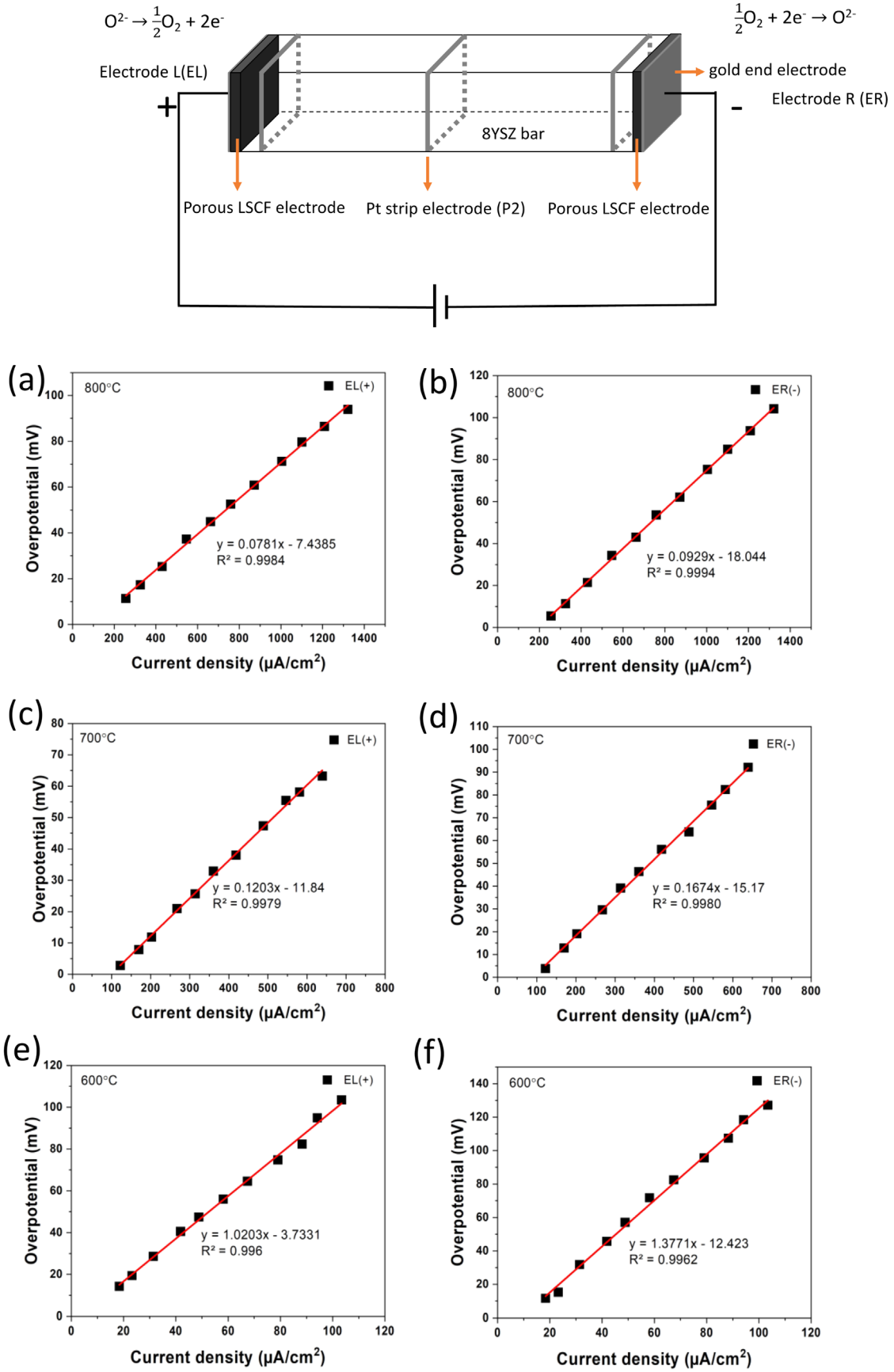

Figure 11. Overpotential vs current density for (a), (c), (e) EL (anode), and (b), (d), (f) ER (cathode) at (a), (b) 600 °C, (c), (d) 700 °C, and (e), (f) 800 °C with the polarity of EL(+) and ER(−).

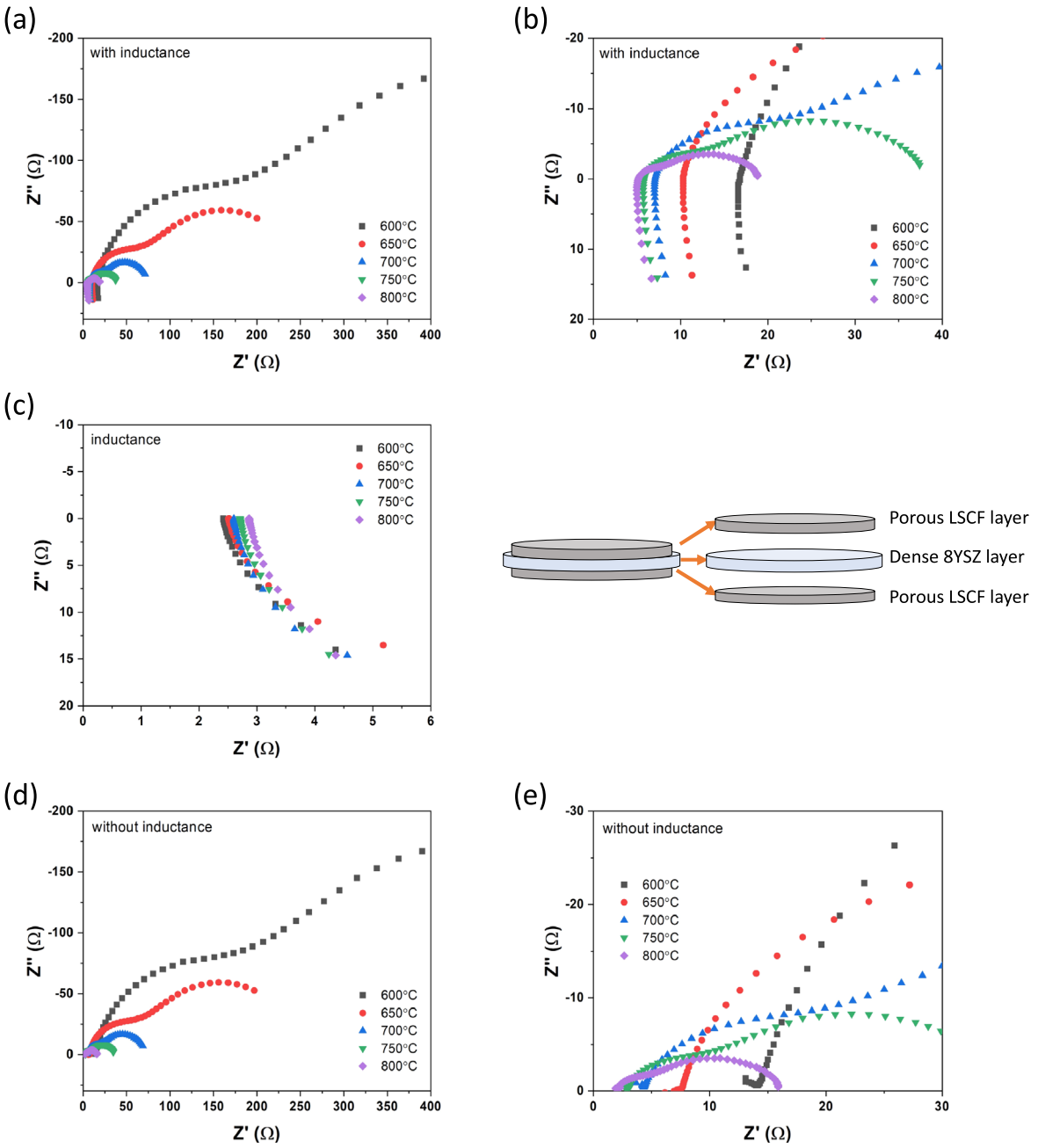

Figure 12. Impedance spectra (a) across the entire sample of the disk-shaped LSCF/8YSZ/LSCF sample, including the sample and the leads resistance/inductance over a temperature range from 600 to 800 °C, (b) an enlarged view of the high frequency region in (a). (c) Leads resistance/inductance over a temperature range from 600 to 800 °C. Impedance spectra (d) across the entire sample of the disk-shaped LSCF/8YSZ/LSCF without leads resistance/inductance over a temperature range from 600 to 800 °C (e) enlarged view of the high frequency region in (d).

polarization resistance will be much greater at current densities much lower than the exchange current density. In PEMFC, this effect is well known. As a result, at a typical operating temperature of 80 °C, the measured cell voltage at OCV is often much lower than the Nernst voltage. The measured cell voltage at OCV will be close to the Nernst voltage only if one uses an impedance meter with a large input impedance (such as an electrometer).[22]

The specific polarization resistance of ~5.2 Ωcm^2 measured on the LSCF/YSZ-disk/LSCF sample is still high compared to composite electrodes containing LSCF and an oxygen ion conductor (e.g. rare earth oxide-doped CeO_2) due to the low oxygen ion conductivity of LSCF. Because of this, the electrode reaction is essentially confined to the electrolyte/LSCF electrode boundary. In composite electrodes with LSCF as a constituent, electrochemical zone is spread out up to a few microns into the electrode from the electrolyte/electrode interface. This substantially lowers the polarization resistance.

Equations 4 and 6 give two limits of the Butler Volmer Eq. 3. Low overpotential in which case the polarization resistance is nearly constant and is inversely proportional to the exchange current density. High overpotential in which the overpotential is proportional to the logarithm of the current density (Tafel limit). We have seen that in results on the bar sample, the maximum current density is much lower than the exchange current density. Correspondingly, the as-determined polarization resistance is much greater than that determined on the YSZ disk sample with identical LSCF electrodes (fired under the same conditions). Figure 13 shows a schematic plot of overpotential vs current density. The polarization resistance

(which varies with current density) is given by $\frac{\eta}{i}$, shown in the figure. One often defines local polarization resistance as $\frac{d\eta}{di}$, also shown in Fig. 13.[28] Limit of $\frac{d\eta}{di}$ as the current density goes to zero, which is also the limit of $\frac{\eta}{i}$, as the current density goes to zero, can be determined as follows.

Starting with the Butler-Volmer equation one can obtain a derivative of the overpotential with respect to current density as

$$\frac{d\eta}{di} = \frac{RT}{i_o zF\left\{(1-\alpha)\exp\left[\frac{(1-\alpha)zF\eta}{RT}\right] + \exp\left[-\frac{\alpha zF\eta}{RT}\right]\right\}} \quad [9]$$

Note that the derivative is obtained by differentiating the Butler-Volmer equation. If one takes the limit of the above as $\eta \to 0$, one obtains $\frac{d\eta}{di} = \frac{RT}{zFi_o}$ regardless of the value of α. An important point is that the limit is obtained as the overpotential approaches zero. Our interest is in obtaining the limit as the current density goes to zero and also as a function of current density. This requires that the overpotential be described as a function of current density; not current density as a function of overpotential, which is what the general Butler-Volmer equation gives. For $\alpha = \frac{1}{2}$, the Butler-Volmer equation is given as a sine-hyperbolic function. Thus, the overpotential can be given as

$$\eta = \frac{2zF}{RT}\sin h^{-1}\left(\frac{i}{2i_o}\right) \quad [10]$$

The above can now be differentiated with respect to current density, which gives

$$\frac{d\eta}{di} = \frac{RT}{i_o zF\sqrt{\left(\frac{i}{2i_o}\right)^2 + 1}} \quad [11]$$

Note that if the current density goes to zero, one obtains $\frac{d\eta}{di} = \frac{RT}{zFi_o}$. Fundamental difference is that Eq. 11 gives derivative of overpotential with respect to current density as a function of current density. From the estimated i_o of 4.2 mAcm^{-2} from the disk sample at 800 °C, now one can estimate $\frac{d\eta}{di}$. From Fig. 10b, corresponding to current density of 1000 ΩAcm^{-2}, the $\frac{d\eta}{di}$ is estimated as ∼10.93 Ωcm^2, while that corresponding to current density of 200 ΩAcm^{-2}, the $\frac{d\eta}{di}$ is estimated as ∼11.00 Ωcm^2. In these estimates, the transfer coefficient, α, was assumed to be 0.5. Equation 11 also shows that for actual current density much greater that the exchange current density, which is the case in a typical fuel cell, the $\frac{d\eta}{di}$ will be much lower, as is typically observed. Note that the observed very linear relationship between overpotential and current density is in good agreement with measurements given Figs. 10 and 11. Given that no information is available about α, and that the electrode reactions are multi-electron, meaning the very applicability of the Butler-Volmer equation may be in question, the above estimates are deemed reasonable.

The electrolyte conductivity and the specific polarization resistance from the EIS data and the DC data obtained on the YSZ bar sample are summarized in Table I. The bulk resistance R_b is estimated from the high frequency intercept of the EIS data, and then the electrolyte conductivity is calculated. The total resistance R_t can be estimated from the low frequency intercept, although one has to extrapolate the low frequency arc to the x-axis in EIS spectra. Assuming both of the arcs in the impedance spectra are from the electrode processes, the total area specific electrode polarization resistance R_{ct} can be calculated as $R_{ct} = R_t - R_b$.[19,22] The

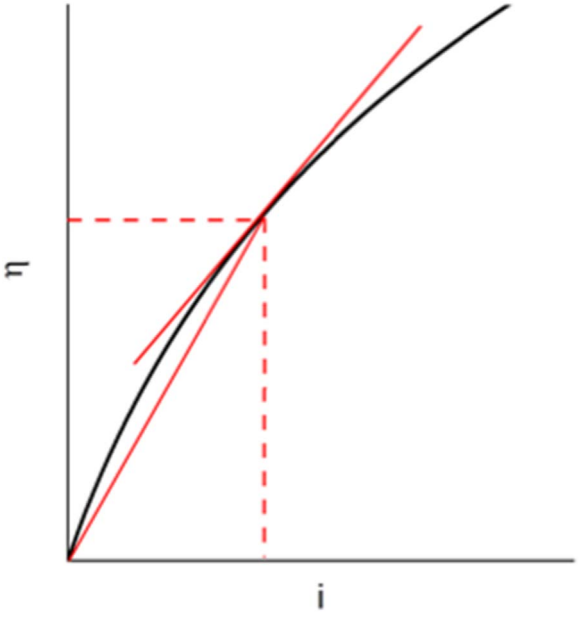

Figure 13. A schematic plot of overpotential vs current density.

electrolyte conductivity from the DC data was calculated from the resistivity obtained from the plot of the YSZ resistance vs distance. The total area specific electrode polarization resistance from the DC data was calculated as the sum of the specific polarization resistances of EL and ER. DC data are in good agreement with the EIS data. Only at 800 °C, the electrolyte resistance and the total area specific polarization resistance from the DC data are slightly larger than that from the EIS data. Again, wide platinum strip electrodes are considered to contribute to the uncertainty. At 800 °C the electrolyte resistance and the total area specific polarization resistance are smaller, and wide platinum strip electrodes may have a greater influence on them. Good agreement in DC and EIS results on the YSZ ionic conductivity also implies that the high frequency intercept does include both YSZ grain and grain boundary contributions on the YSZ bar sample. That is, the grain boundary capacitance was not shorted at the highest frequency used in the EIS measurements. Alternatively, the YSZ grain boundary resistance is relatively small at and above 600 °C.

Figure 14 shows Arrhenius plots of (a) the electrolyte conductivity and (b) the total area specific electrode polarization resistance by EIS (black) and DC (red) tests. Both the electrolyte conductivity and the total area specific electrode polarization resistance exhibit Arrhenius relations given by Eqs. 12 and 13, respectively.

$$\sigma T = \sigma_o \exp\left[\frac{-E_a}{k_B T}\right] \quad [12]$$

$$\frac{R_{ct}}{T} = R_o \exp\left[\frac{E_{ct}}{k_B T}\right] \quad [13]$$

In these equations, σ is the electrolyte conductivity, R_{ct} is the specific polarization resistance, σ_o and R_o are the pre-exponential factors, E_a is the activation energy for ion diffusion in YSZ, E_{ct}, is the activation energy for the polarization resistance, k_B is the Boltzmann constant, and T is the absolute temperature. Both the Arrhenius plots of the electrolyte conductivity and the total area specific electrode polarization resistance show linear relationships in the Arrhenius plots over the measured temperature range. The activation energies for the electrolyte conductivity obtained from the EIS data and DC tests are 0.95 and 1.03 eV, respectively. The activation energies for the total area specific electrode polarization

Table I. Comparison of measurements from EIS and DC tests.

Temperature (°C) and polarity		Electrolyte conductivity from EIS data (σ, Scm^{-1})	Electrolyte conductivity from DC data (σ, Scm^{-1})	Total Area specific electrode polarization resistance from EIS data (R_{ct}, Ωcm^2)	Total area specific electrode polarization resistance from DC data (R_{ct}, Ωcm^2)
800	EL (−)-ER (+)	2.7×10^{-2}	3.3×10^{-2}	124.7	172.3
	ER (+)-EL (−)	2.7×10^{-2}		131.0	171.0
700	EL (−)-ER (+)	1.5×10^{-2}	1.2×10^{-2}	298.1	297.2
	ER (+)-EL (−)	1.5×10^{-2}		300.5	287.7
600	EL (−)-ER (+)	3.2×10^{-3}	3.2×10^{-3}	2493.7	2442.1
	ER (+)-EL (−)	3.3×10^{-3}		2511.2	2397.4

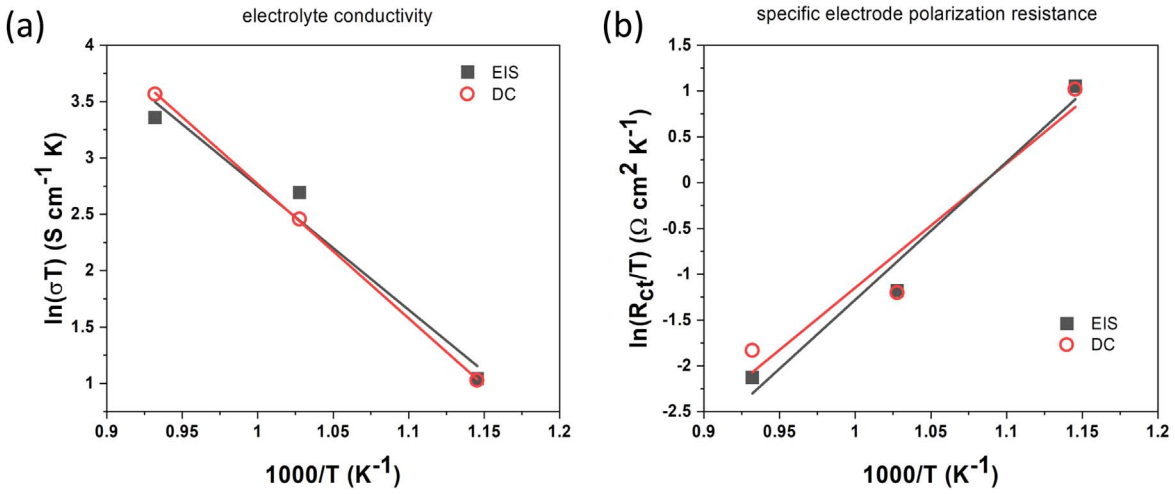

Figure 14. Arrhenius plots of (a) the electrolyte conductivity and (b) the total area specific electrode polarization resistance by EIS (black) and DC tests (red).

resistance obtained from the EIS data and the DC tests are 1.30 eV and 1.17 eV, respectively. EIS and DC measurements, thus, show good agreement with each other.

As stated earlier, Szendrei et al.[23] measured a much higher polarization resistance for the ORR than for the OER when using LSM + YSZ as the electrodes. LSM is essentially an electronic conductor. The reactions $\frac{1}{2}O_2 + 2e' \rightarrow O^{2-}$ and $O^{2-} \rightarrow \frac{1}{2}O_2 + 2e'$ occur at LSM/YSZ/gas phase TPB. With LSCF alone as an electrode, the reactions occur some on the two phase (LSCF/gas) surface and some at the gas phase/LSCF/YSZ TPB limited to the electrolyte/electrode interface. These differences may lead to differences in the polarization resistances for the two reactions in these two different systems.

Conclusions

Electrolyte resistance and specific polarization resistance were measured on a cell consisting of LSCF electrodes and an electrolyte consisting of an 8YSZ bar using both EIS and DC techniques. Platinum strip electrodes were applied perpendicular to the length of the YSZ bar for potential measurements. Two-electrode EIS with three probes was used to study the electrode kinetics of the cathode and the anode separately. The impedance spectra across EL and P2 are slightly different from the impedance spectra across ER and P2. When the polarity is switched, the impedance spectra across EL and P2 and across ER and P2 do not change. The polarization resistance of each electrode was, thus, not affected by the polarity. But the results indicate that the two electrodes need not be identical. Some differences were observed and this needs to be studied further. A point-by-point sum of the impedance spectra across EL and P2 and across ER and P2 matches the impedance spectra across EL and ER. By utilizing a pseudo-reference electrode and the measured resistivity, DC tests were also used to measure the polarization resistances of the two electrodes separately. EIS and DC measurements are in good agreement with each other. EIS was also conducted on a LSCF/YSZ/LSCF disk-shaped sample with YSZ disk thickness of ~0.8 mm. The measured specific polarization resistance was much lower. The unusually high specific polarization resistances measured on the bar sample were attributed to the regime of exceptionally low current densities (much lower than the exchange current density) explored in the experiments. The present approach thus allows the measurement of electrode kinetics at operating current densities much lower than the exchange current density.

Acknowledgments

This work was supported by the National Science Foundation under grant numbers NSF-CBET-1604008 and NSF-DMR-1742696.

ORCID

Michael F. Simpson https://orcid.org/0000-0002-0099-0097

References

1. E. Perry Murray, T. Tsai, and S. A. Barnett, "A direct-methane fuel cell with a ceria-based anode." *Nature*, **400**, 649 (1999).
2. A. Esquirol, N. P. Brandon, J. A. Kilner, and M. Mogensen, "Electrochemical characterization of La0.6Sr0.4Co0.2Fe0.8O_3 cathodes for intermediate-temperature SOFCs." *J. Electrochem. Soc.*, **151**, A1847 (2004).
3. M. Liu, Z. Liu, M. Liu, and L. Yang, "LSM-infiltrated LSCF cathodes for solid oxide fuel cells." *J. Energy Chem.*, **22**, 555 (2013).
4. L. Zhang, L. Zhu, and A. V. Virkar, "Nanostructured cathodes for solid oxide fuel cells by a solution spray-coating process." *J. Electrochem. Soc.*, **163**, F1358 (2016).
5. N. Q. Minh, "Solid oxide fuel cell technology-features and applications." *Solid State Ionics*, **174**, 271 (2004).
6. P. Singh and N. Q. Minh, "Solid oxide fuel cells: technology status." *Int. J. Appl. Ceram. Technol.*, **1**, 5 (2004).
7. J. Liu and S. A. Barnett, "Operation of anode-supported solid oxide fuel cells on methane and natural gas." *Solid State Ionics*, **158**, 11 (2003).
8. J. M. Ralph, C. Rossignol, and R. Kumar, "Cathode materials for reduced-temperature SOFCs." *J. Electrochem. Soc.*, **150**, A1518 (2003).
9. M. Mogensen, "The kinetics of hydrogen oxidation on a Ni-YSZ SOFC Electrode at 1000 °C." *ECS Proc.*, **1993–4**, 484 (1993).
10. T. Van Gestel, D. Sebold, and H. P. Buchkremer, "Processing of 8YSZ and CGO thin film electrolyte layers for intermediate- and low-temperature SOFCs." *J. Eur. Ceram. Soc.*, **35**, 1505 (2015).
11. H. Huang, M. Nakamura, P. Su, R. Fasching, Y. Saito, and F. B. Prinz, "High-Performance Ultrathin solid oxide fuel cells for low-temperature operation." *J. Electrochem. Soc.*, **154**, B20 (2007).
12. T. Suzuki, M. Awano, P. Jasinski, V. Petrovsky, and H. U. Anderson, "Composite (La, Sr)MnO_3-YSZ cathode for SOFC." *Solid State Ionics*, **177**, 2071 (2006).
13. X. Luo, Y. Yang, Y. Yang, D. Tian, X. Lu, Y. Chen, Q. Huang, and B. Lin, "Reduced-temperature redox-stable LSM as a novel symmetrical electrode material for SOFCs." *Electrochim. Acta*, **260**, 121 (2018).
14. T. Fukui, K. Murata, S. Ohara, H. Abe, M. Naito, and K. Nogi, "Morphology control of Ni-YSZ cermet anode for lower temperature operation of SOFCs." *J. Power Sources*, **125**, 17 (2004).
15. B. Fan, J. Yan, and X. Yan, "The ionic conductivity, thermal expansion behavior, and chemical compatibility of La0.54Sr0.44Co0.2Fe 0.8O_3-δ as SOFC cathode material." *Solid State Sci.*, **13**, 1835 (2011).
16. H. Hidalgo, A. L. Thomann, T. Lecas, J. Vulliet, K. Wittmann-Teneze, D. Damiani, E. Millon, and P. Brault, "Optimization of DC reactive magnetron sputtering deposition process for efficient YSZ electrolyte thin film SOFC." *Fuel Cells*, **13**, 279 (2013).
17. S. P. Jiang, "A comparison of O_2 reduction reactions on porous (La,Sr)MnO_3 and (La,Sr)(Co,Fe)O_3 electrodes." *Solid State Ionics*, **146**, 1 (2002).
18. L. W. Tai, M. M. Nasrallah, H. U. Anderson, D. M. Sparlin, and S. R. Sehlin, "Structure and electrical properties of la1-xSrxCo1-yFeyO_3. part 2. the system la1-xSrxCo0.2Fe0.8O_3." *Solid State Ionics*, **76**, 273 (1995).
19. M. Liu and Z. Wu, "Significance of interfaces in solid-state cells with porous electrodes of mixed ionic-electronic conductors." *Solid State Ionics*, **107**, 105 (1998).
20. N. Wagner, W. Schnurnberger, B. Müller, and M. Lang, "Electrochemical impedance spectra of solid-oxide fuel cells and polymer membrane fuel cells." *Electrochim. Acta*, **43**, 3785 (1998).
21. A. Szendrei, T. D. Sparks, and A. Virkar, "Three and four-electrode electrochemical impedance spectroscopy studies using embedded composite thin film pseudo-reference

electrodes in proton exchange membrane fuel cells." *J. Electrochem. Soc.*, **166**, F784 (2019).
22. A. Szendrei, T. D. Sparks, and A. V. Virkar, "Measurement of ionic conductivity and electrode polarization at low temperatures on 8YSZ by a DC technique." *J. Electrochem. Soc.*, **164**, F1543 (2017).
23. A. Szendrei, T. D. Sparks, and A. V. Virkar, "Measurement of polarization resistance of LSM + YSZ electrodes on YSZ using AC and DC methods." *ECS Trans.*, **91**, 1363 (2019).
24. L. Zhang, F. Liu, K. Brinkman, K. L. Reifsnider, and A. V. Virkar, "A study of gadolinia-doped ceria electrolyte by electrochemical impedance spectroscopy." *J. Power Sources*, **247**, 947 (2014).
25. L. Zhang, L. Zhu, and A. V. Virkar, "Electronic conductivity measurement of yttria-stabilized zirconia solid electrolytes by a transient technique." *J. Power Sources*, **302**, 98 (2016).
26. X. J. Chen, K. A. Khor, S. H. Chan, and L. G. Yu, "Influence of microstructure on the ionic conductivity of yttria-stabilized zirconia electrolyte." *Mater. Sci. Eng. A*, **335**, 246 (2002).
27. G. Raikova, P. Carpanese, Z. Stoynov, D. Viadikova, M. Viviani, and A. Barbucci, "Inductance correction in impedance studies of solid oxide fuel cells." *Bulg. Chem. Commun.*, **41**, 199 (2009).
28. N. Wagner, "Characterization of membrane electrode assemblies in polymer electrolyte fuel cells using a.c. impedance spectroscopy." *J. Appl. Electrochem.*, **32**, 859 (2002).